

Numerical simulation of 3-D mantle flow evolution in subduction zone environments in relation to seismic anisotropy beneath the eastern Mediterranean region

Judith M. Confal^{a,*}, Manuele Faccenda^b, Tuna Eken^a, Tuncay Taymaz^a

^a*Department of Geophysical Engineering, The Faculty of Mines, Istanbul Technical University, 34469 Maslak, Sariyer, Istanbul, Turkey*

^b*Department of Geoscience, University of Padua, Italy*

Abstract

Seismic anisotropy is a key parameter in understanding subduction zone dynamics in relation to the recent deformation history. It is usually controlled by the mantle flow patterns resulting from the dynamic interactions between a relatively dense subducting oceanic plate and the surrounding mantle. A proper modelling of mantle flow in subduction systems helps our understanding of the seismic anisotropy source, strength and evolution in time. This study further examines shear wave splitting parameters, one of the most well established measuring methods of seismic anisotropy, and their anisotropy source, based on 3-D geodynamic modelling, applied to the eastern Mediterranean Sea and Anatolia. Our model setting is chosen to be a first order representation of the present-day tectonic setting as it consists of a deforming Anatolian micro-plate, that is indented by slow moving African and Arabian plates, and an oceanic plate in between. The retreat of the slab in the Aegean region, the alleged tear in the subducting slab close to the Cyprus trench and the break-off in the slab in eastern Anatolia are considered in our modelling study in order to further explore their influence on mantle flow and splitting parameters. The synthetically calculated fast polarization directions (FPDs) mostly showed a reasonable matching with those inferred from previous seismological observations that are mainly SKS splitting measurements. Regions of FPD similarities between synthetic and observed shear waves mostly indicate N-S to NE-

*Corresponding author

Email address: judithconfal@gmail.com (Judith M. Confal)

SW orientations of fast shear waves, which are parallel to the extension in the back-arc region and in general perpendicular to the trench. The pattern of FPDs seems to be more complex nearby the trench. Our modelling results suggest that the development of a tear in the African slab and the detachment occurring within the Arabian plate (break-off) appear to have a significant influence on the FPDs due to stronger mantle flow through the slab windows. The mantle flow through the tear close to Cyprus and the break-off in the East can be identified clearly, despite their recent appearances. A circular pattern around the edges of the slab can be observed as well as disruptions of the overall general fast polarization direction due to the flow through the tear.

Keywords: Aegean; Eastern Mediterranean; Kinematics of upper mantle deformation; Numerical modelling; Seismic anisotropy; Shear wave splitting; Subduction zone processes

1. Introduction

A proper modelling of 3-D mantle flow evolution beneath the eastern Mediterranean, the Aegean and Anatolia, will significantly contribute to our understanding of the complex dynamics of this region, involving subduction zones, back-arc spreading, collisional and extrusion tectonics (Fig. 1). Indeed, by having a proper knowledge of upper mantle flow history, recent kinematics and dynamic patterns of the mantle can be reconstructed (e.g. Faccenna et al., 2013; Sternai et al., 2014). Comparing synthetic data with observational constraints, i.e., from seismic anisotropy, tomographic models and geodetic measurements, can comprehensively help us to illuminate the evolution of mantle flow patterns as well as their influence on subduction zone environments (e.g. Park & Levin, 2002). Seismic anisotropy, generated by strain-induced lattice preferred orientations (LPOs) of olivine, the most abundant mineral in the upper mantle, is widely used to infer upper mantle flow characteristics. Observations on the splitting of shear waves into fast and slow components are the most common and direct approach to recover a path-integrated fast wave orientation and the strength of anisotropy. The fast wave is orthogonal to the slow one and is polarized in the plane with the highest shear wave velocity (fast polarisation direction, FPD). The time delay (TD) between

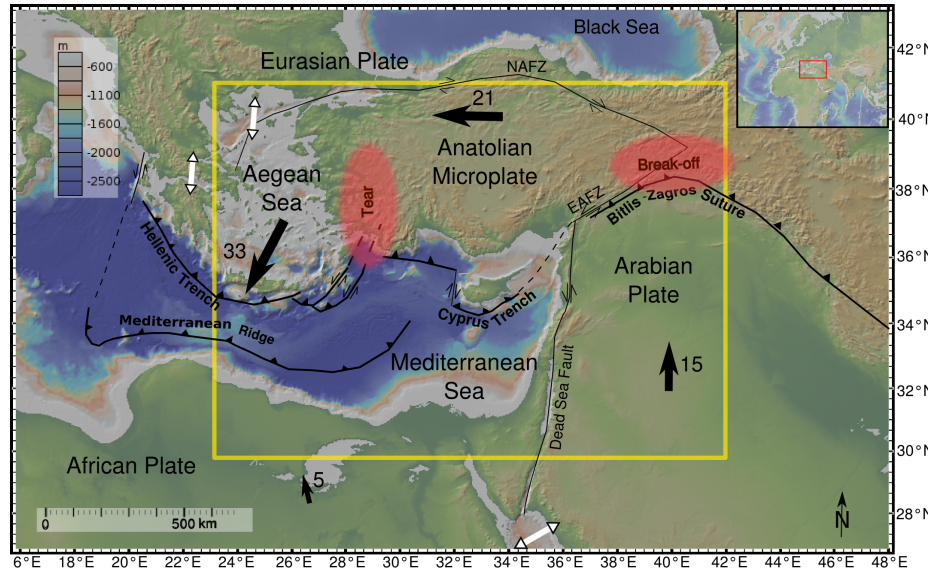


Figure 1: Active tectonic map of the eastern Mediterranean (Global Multi-Resolution Topography map from GeoMapApp, <http://www.geomapapp.org>) and sketch of main active tectonic features after Dilek & Altunkaynak (2009, and references therein) with principal movements of the plates in respect to a stable Eurasian plate after Le Pichon & Kreemer (2010). Black solid arrows show directions of plate movements with their respective plate velocities in mm/yr and white arrows represent extensional regimes (about 15 mm/yr in the North Aegean and the Gulf of Corinth and 17 mm/yr in the Red Sea). The yellow square represents the modelled region. The transparent red areas show the supposed locations of the slab tear in western Turkey and the slab break-off in eastern Turkey. Lines with triangles show thrust faults and subduction zones, normal lines with paired arrows are strike slip boundaries. NAFZ and EAFZ represent the North and East Anatolian Fault Zones, respectively.

18 the fast and slow wave is proportional to the thickness and the intrinsic anisotropy
 19 of the medium the shear wave is propagating through. Early studies (Long & Silver,
 20 2009) tend to link flow patterns with the distribution of anisotropy that were inferred
 21 mainly from SKS, SKKS and local/teleseismic S waves. A global compilation of split-
 22 ting observations has indicated that the FPDs in subduction systems are mostly trench-
 23 perpendicular in the back-arc region and trench-parallel closer to the trench (Long &
 24 Silver, 2009).

25 Apart from mantle flow patterns, Karato et al. (2008) claimed that other parameters
 26 such as temperature, water content and deviatoric stress influence the LPO of olivine.

27 Apparent anisotropy, related to isotropic compositional heterogeneities, could consti-
 28 tute an additional anisotropy source (e.g. Babuska & Cara, 1991). Traditionally, mod-
 29 elling studies assume time-independent, steady-state flow dynamics to calculate mantle
 30 fabrics and the associated anisotropy (e.g. Becker, 2006). This method has been shown
 31 to be effective in global intra-oceanic settings (e.g. Pacific and Atlantic ocean) where
 32 plate motions and shallow mantle flow has been stable over the past 43 Myrs (Faccenna
 33 et al., 2013, e.g.). Recently, (Faccenda & Capitanio, 2013, and references therein) have
 34 extended this methodology to account for the non-steady state deformation, likely to
 35 be expected at subduction zones, characterized by trench and slab lateral migration.
 36 Faccenda & Capitanio (2013) identified two types of anisotropic domains in the mod-
 37 elled sub-slab mantle: trench-parallel in the deeper upper mantle related to the diverg-
 38 ing toroidal mantle flow component, and trench-perpendicular within the overlying and
 39 dip-parallel mantle that is entrained at depth by the subducting plate. Another signif-
 40 icant result from their model is, that the strength of sub-slab trench-parallel splitting
 41 directions are prone to be manifested by the amount of the retreat motion rather than
 42 the migration rate of the slab. Faccenda & Capitanio (2013), modelled the upper mantle
 43 anisotropy for 3-D subduction models with different geometries. Synthetically com-
 44 puted splitting parameters agree overall with observations from different subduction
 45 zones if the mantle flow (and thus the olivine fast axis) is sub-horizontal, while the fit
 46 degrades in proximity to the trench, where the flow is dipping parallel to the slab. In
 47 particular, their study was successful in modelling the circular FPD pattern at the edges
 48 of a subducting slab and the trench-perpendicular FPDs in the back-arc regions. The
 49 trench-parallel FPDs commonly observed at fore-arcs were reproduced only in mod-
 50 els that develop a strong sub-slab trench-parallel fabric in response to a sustained slab
 51 roll-back and pure shear deformation (Faccenda & Capitanio, 2013).

52 Our aim in this study is to apply a similar modelling approach to the complicated
 53 eastern Mediterranean subduction system, where the present-day geological setting
 54 (Fig. 1) shows an African plate subducting underneath a stable Eurasia and a fast mov-
 55 ing Anatolian microplate (Reilinger et al., 2006). In the initial model set up, we con-
 56 sider crustal thicknesses, widths of plates, Moho depths and the expected time frame of
 57 the subduction process, based on available literature for a realistic approach, to model

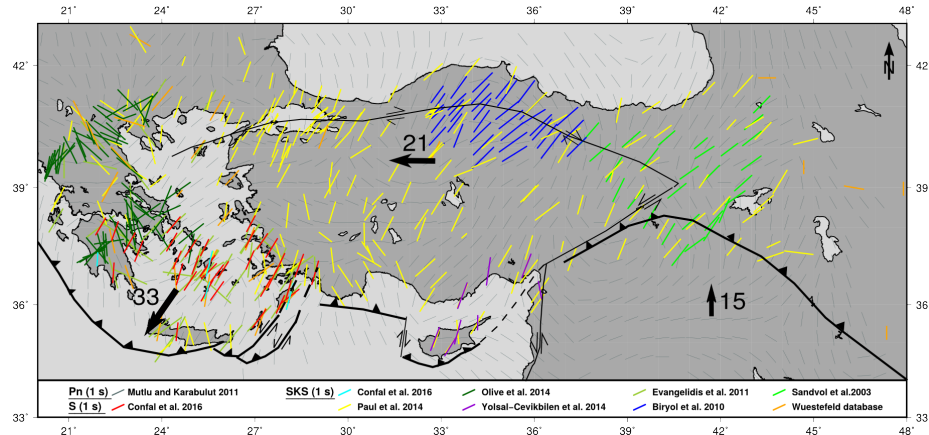


Figure 2: Anisotropy parameters from previous Pn-tomography (Mutlu & Karabulut, 2011), direct S-wave (Confal et al., 2016) and SKS-wave studies in the eastern Mediterranean from the splitting data base of Wüstefeld & Bokermann (2007) and (Sandvol et al., 2003; Biryol et al., 2010; Evangelidis et al., 2011; Yolsal-Çevikbilen, 2014; Paul et al., 2014; Olive et al., 2014; Confal et al., 2016). Black solid arrows show directions of plate movements with their respective plate velocities in mm/yr.

the geodynamics of the region. However, it is also important to note that this study of-
fers only a first order approximation of the presumed mantle flow and strain pattern in
the mantle in relation to the shear-wave splitting parameters, rather than exploring the
exact geodynamic evolution of the subduction process and its corresponding tectonic
setting in the eastern Mediterranean region.

1.1. Tectonic setting of the region

The eastern Mediterranean region is one of the most tectonically active regions in
the world. Following the convergence of Africa and Eurasia, the Ionian oceanic litho-
sphere continues to subduct beneath Eurasia while the Anatolian plateau escapes west-
wards. The region is characterized by two different active subduction systems (Cyprus
and Hellenic), a collision zone around the Bitlis-Zagros suture, an extensional region
in the Aegean Sea, and an extruding Anatolian microplate (e.g. Le Pichon & Kreemer,
2010).

Tectonic history reconstructions of Van Hinsbergen et al. (2005) dated the closing of
the Pindos (Neo-Tethys) ocean at around 34 Myrs. Seismic tomography, geological

73 models and 3-D numerical models (e.g. Wortel & Spakman, 2000; Jolivet & Faccenna,
 74 2000; Menant et al., 2016) suggest that the extension in the northern Aegean started
 75 in the Oligocene-Miocene around 25 to 35 Myrs ago and the recent phase of exten-
 76 sion is about 10-15 Myrs old (Wortel & Spakman, 2000). Govers & Fichtner (2016)
 77 proposed a fragmentation of the slab in the Eocene-Miocene, leading to the roll-back
 78 in the Aegean (Hellenic slab) and the steepening of the Cyprus slab based on 3-D
 79 high-resolution S-wave speed distribution in the region. Jolivet et al. (2015) dated the
 80 beginning of slab tearing close to the Cyprus trench at around 15 Myrs, due to fast ex-
 81 tension. Low velocity anomalies, resolved in southwestern Turkey, based on body and
 82 surface wave tomography studies (Taymaz, 1996; Biryol et al., 2011; Govers & Ficht-
 83 ner, 2016), tend to support the idea of a North-South vertical tear within the African
 84 slab, which propagates laterally. Low velocity anomalies, from 50-100 km down to
 85 a depth of about 800 km evidenced the indication of this tear in the slab between the
 86 Cyprus and the Hellenic trench. Moreover, there might be even evidence for a smaller
 87 tear in the Cyprus trench (Biryol et al., 2011). A steepening of the African slab from
 88 the west to the east in the Aegean Sea is evident from tomography images (e.g. Wortel
 89 & Spakman, 2000).

90 On the basis of the reconstruction of geodynamic evolution, Jolivet & Faccenna (2000)
 91 claimed that Anatolia and Arabia collided around 30 to 35 Myrs ago. In the East, where
 92 the Anatolian and the Arabian plate collide, the common consensus at the moment is
 93 that a break-off of the Arabian slab is mainly responsible for the formation of the east
 94 Anatolian plateau (domal uplift) and volcanism (e.g. Keskin, 2003). He describes the
 95 Anatolian crust being still actively deforming, while the northward subducting oceanic
 96 lithosphere of the Arabian plate steepened, the mantle lithosphere delaminated (Göğüş
 97 & Pysklywec, 2008) and parts of the slab detached itself from the accretionary wedge.
 98 Keskin (2003) dates the initiation of the break-off around 11-13 Myrs ago. A recent
 99 high resolution S-receiver function study performed by Kind et al. (2015) indicated
 100 that the seismological lithosphere-asthenosphere boundary (LAB) could not be deeper
 101 than 100-120 km in eastern Turkey. Faccenna et al. (2006) interpreted the sharp tran-
 102 sition between fast and slow Pn-velocities around the Central Anatolian Fault Zone as
 103 the edge of a second slab window, continuing to the west. For modelling purposes we

will consider the widely accepted theory of just one slab window in the East below the collision zone.

Pasyanos & Walter (2002) obtained crustal thicknesses for the African plate around 40 km and for the Arabian plate 25-35 km. The Anatolian plate is about 30 km thick in the West (e.g. Vanacore et al., 2013, and references therein), 37-47 km in central Anatolia and 38-55 km thick on the eastern Anatolian Plateau, as it simply indicates a west-to-east crustal thickening (e.g. Mutlu & Karabulut, 2011; Vanacore et al., 2013). Due to the retreat the crust of the Aegean Sea is thinner (about 25 km, (Tirel et al., 2004) than surrounding plates.

Geodetic observations showed a northward movement of Africa, by about 5 mm/yr with respect to Eurasia and 15 mm/yr for the Arabian plate (Reilinger et al., 2006; Le Pichon & Kreemer, 2010). The Anatolian plate rotates counterclockwise at around 18-25 mm/yr and the Aegean domain migrates at about 33 mm/yr to the southwest. A proper understanding of the relative contribution to the present-day active deformation from both the continental collision of the Arabian and Eurasian plate triggering a westward material extrusion in Anatolia (e.g. Le Pichon & Kreemer, 2010) and the pull in the West due to the fast extension in the Aegean domain still remains debated (e.g. Sternai et al., 2014). At present it is evident from geodetic observations that the retreat of the southwestward dipping Hellenic slab produces an extensional regime of about 15 mm/yr in the Aegean Sea. Faccenna et al. (2003) favoured the orogenic collapse model, triggered by slab roll-back as the origin of the fast extension. Jolivet et al. (2013, and references therein) enhanced this theory by adding slab tearing, which became more plausible in recent years owing to the advances in GPS technology. In this study we consider the roll-back mechanism as an influential parameter on the mantle flow dynamics.

1.2. Anisotropic pattern of the region

Early SKS- and S-wave splitting studies performed in the eastern Mediterranean and Anatolia (Sandvol et al., 2003; Biryol et al., 2010; Evangelidis et al., 2011; Paul et al., 2014; Olive et al., 2014; Yolsal-Çevikbilen, 2014; Confal et al., 2016) have

134 clearly indicated almost consistent NE-SW oriented anisotropic directions in the up-
 135 per mantle and crust with sub-lithospheric origin (Fig. 2). In the western part of the
 136 study area and back-arc region FPDs are mostly NNE-SSW oriented with high TDs,
 137 while FPDs become rather NE-SW directed to the east and far from the trench with
 138 lower TDs. In southwestern Turkey, where the tear in the slab is suspected, the lat-
 139 eral variations of splitting parameters become more complicated (Paul et al., 2014).
 140 The dominant characteristics of the FPD distribution in the Aegean Sea is a trench-
 141 perpendicular pattern. Furthermore, Evangelidis et al. (2011) found a trench-parallel
 142 FPD pattern in the fore-arc region of the Aegean, but this is not supported by recent
 143 studies (Paul et al., 2014; Confal et al., 2016). On the Peloponnes and the Greek
 144 mainland Olive et al. (2014) and Evangelidis (2017) observed very complex trench-
 145 normal/parallel FPDs structures. They argue that these patterns are mainly affected
 146 by local changes beneath and above the slab due to return flow. Trench-parallel FPDs
 147 in the fore-arc region at shallow depth (<50 km) and trench-normal FPDs in sub-slab
 148 depths at the trench, might indicate a tear in the lower slab (Evangelidis, 2017).
 149 Based on anisotropic inversion of surface waves, Endrun et al. (2011) revealed N-S di-
 150 rected, strain-related anisotropy parallel to the extension in the lithosphere of the north-
 151 ern Aegean and NE-SW directed anisotropy in the central Aegean crust from Miocene
 152 paleo-extension. A tomography study by Çubuk-Sabuncu et al. (2017) reported strong
 153 radial anisotropy throughout the crust of western Turkey and Mutlu & Karabulut (2011)
 154 observed that fast directions of Pn waves in the crust are consistent with SKS- and S-
 155 wave studies, especially in the central Aegean Sea, eastern Anatolia and central Turkey.
 156 Small differences, especially close to the trench, in the northern part of the Anatolian
 157 plate and western Turkey are prominent since active tectonics strongly affect Pn-waves
 158 in the crust.

159 **2. Numeric modelling**

160 Following the first 2-D steady-state models, dynamic recrystallisation and plastic
 161 deformation were included to study strain-induced anisotropy in the upper mantle (e.g.
 162 Becker, 2006), but the mantle flow is still seen as steady-state. These methods are

163 problematic when it comes to subduction zones, which develop and change the flow
164 pattern over their evolution. In this study, we apply the numerical modelling method,
165 first introduced and modified for inter-compatibility of various modelling steps, com-
166 putational speed, 3-D Cartesian geometry and time varying strain-induced anisotropy
167 by Faccenda & Capitanio (2013). To calculate shear wave splitting parameters, it con-
168 sideres the full development of the mantle flow and anisotropy in the upper mantle that
169 has resulted from the recent evolution of slab roll-back and tearing (about 30 Myrs)
170 within the eastern Mediterranean subduction zone system. Prior to calculating SKS
171 splitting parameters, two modelling steps are performed.

172 *2.1. Mantle flow modelling*

173 3-D petrological-thermo-mechanical models of subduction have been carried out
174 with I3MG, which is based on a mixed Eulerian-Lagrangian Finite Difference scheme
175 (Gerya, 2009; Faccenda, 2014). We set up a model resembling to a first order the
176 subduction of a branch of the Neo-Tethys ocean (subducting oceanic plate), which
177 still subducts in the eastern Mediterranean region along the Hellenic trench underneath
178 Eurasia (overriding continental plate) and continues east towards the collisional area of
179 the Anatolian and Arabian continental plates.

180 Our model has dimensions of $(x,y,z) = 5000 \times 700 \times 2500$ km (245x69x149 nodes and
181 about 20.4x10.2x16.8 km spatial resolution), with y being the vertical direction. In the
182 initial model (Fig. 3) the lithosphere reaches 90 km depth, as being consistent with
183 the 80-100 km lithospheric thickness modelled beneath Anatolia by Kind et al. (2015)
184 and is a common assumption in geodynamic modelling studies in the region (e.g. Ster-
185 nai et al., 2014). Crustal thicknesses used for continental and oceanic crusts in our
186 study are primarily based on Pasyanos & Walter (2002). Detailed layer thicknesses
187 and informations for each layer can be found in Table 1. The subducting continental
188 plate (representing Arabia) has a crustal thickness of 40 km, a width of 700 km and
189 is 1000 km longer than the plate occupying the remaining part (representing Africa),
190 which has a width of 1800 km. The subducting oceanic crust is 15 km thick, due to res-
191 olution restrictions. Brittle weakening is imposed to ensure lubrication at plate bound-
192 aries. The oceanic plate terminates with a 200 km long slab dipping at about 30° un-

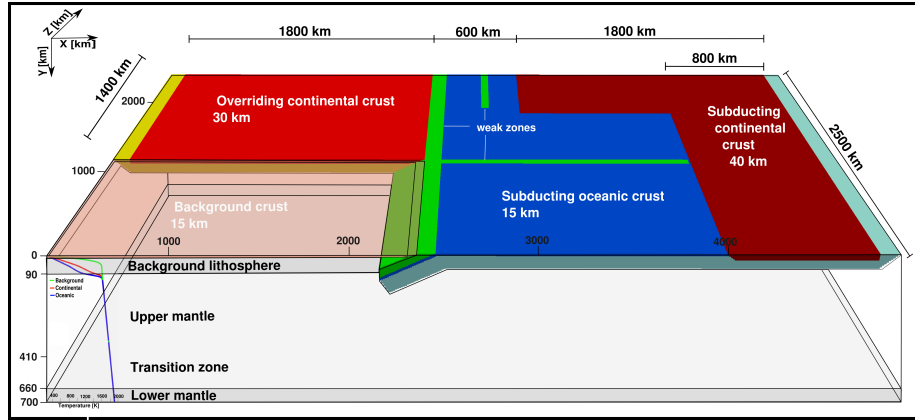


Figure 3: Initial model set-up and compositions of the plates. Widths and thicknesses of the plates are indicated in km. Weak zones are shown in light green. Yellow and light blue layers resemble the lithospheric mantle of the overriding and subducting plates, respectively. The geotherms for the 150 Myrs old oceanic plate (blue), 70 Myrs old overriding continental plate and 5 Myrs old background (green) are shown in the lower left corner of the model.

193 derneath a continental plate (representing Anatolia). A weak lithosphere (background
 194 lithosphere), that facilitates retreat and lateral extrusion of the upper plate (background
 195 crust) is representing the stretched and hot back-arc lithosphere of the Aegean do-
 196 main. The background crust is placed everywhere, except when another continental
 197 or oceanic plate is defined. The overriding continental crust (representing Anatolia) is
 198 30 km thick, 1400 km wide and 1800 km long. A weak zone (100 km width) has been
 199 inserted between the overriding and the subducting plates to reduce the friction in the
 200 subduction channel and facilitate subduction initiation (Sternai et al., 2014). In some
 201 models, two further weak zones (50 km width) are positioned in the areas where the
 202 tear in the slab in western Turkey is located and in front of the shore of eastern Turkey,
 203 to initiate the detachment during the subduction. They were placed according to the
 204 models, giving the best fit to the present-day location of the tear and break-off in the
 205 slab (Biryol et al., 2011). Relative convergence between the two plates is modelled
 206 by imposing a constant velocity (2 cm/yr) on the subducting plate ($z = 0\text{-}2500$ km) and
 207 by fixing the overriding continental plate at the rear ($z = 1875\text{-}2500$ km). The bound-
 208 aries are periodic, normal to the x direction, no slip is imposed at the bottom boundary

209 and free slip to the sides and top boundaries (Faccenda & Capitanio, 2013; Faccenda,
210 2014).

211 The thermal structure (Fig. 3) of the plates is calculated with the half-space cooling
212 model (Gerya, 2009) down to 90 km, below a constant thermal gradient of 0.5 K/km
213 is assumed. The upper plate is set to be 70 Myrs old in the continental portion (over-
214 riding) and 5 Myrs for the background lithosphere, which ensures its deformation and
215 trench retreat, while the subducting and oceanic plate is 150 Myrs old. The oceanic
216 crust, as well as the mantle and background crust have a visco-plastic rheology, based
217 on deformation invariants (Ranalli, 1995; Faccenda, 2014). It has been modelled with
218 wet Quartzite and dry Olivine flow laws, respectively (Table 1). The lower and upper
219 cut-off values of the effective viscosities are 10^{18} and 10^{24} Pa s, respectively. To fur-
220 ther decrease the strength of the upper plate material, its upper cut-off value has been
221 set to 10^{22} Pa s (Table 1). Density is computed as a function of the local P-T diagram
222 generated with PERPLE_X (Connolly, 2005) for a pyrolytic mantle composition. The
223 low friction coefficient of the overriding continental plate (0.01) is needed to ensure
224 yielding of the upper plate due to the used low numerical resolution that does not allow
225 to localize deformation and behaves as a rigid block.

226 2.2. *Mantle fabric modelling*

227 The lattice preferred orientation (LPO) of mantle aggregates are modelled by using
228 a modified version of D-REX (Kaminski et al., 2004). A detailed explanation for the
229 LPO modelling can be found in Faccenda & Capitanio (2013). The Eulerian velocity
230 gradient field from the large-scale mantle flow model is used to compute the fabric de-
231 velopment of each crystal aggregate with an initial spacing of $(x,y,z) = 50 \times 30 \times 50$ km at
232 each time step. Since this study focuses on seismic SKS phase splitting as an observa-
233 tional constraint, we only model the anisotropy in the upper mantle (from the Moho to
234 the 410 km discontinuity) to which the long period S-waves are sensitive. Thus, below
235 410 km no fabric is calculated, but the aggregates continue to be advected with their
236 fabric reset. When emerging in the upper mantle (above 410 km) again a new fabric is
237 computed. Each upper mantle aggregate consists of 1000 randomly oriented crystals
238 (70 % olivine, 30 % pyroxene). We have used the standard D-Rex parameters to cal-

Table 1: Rheological parameters of the different layers. A_D , n , E and V are flow law parameters after (Ranalli, 1995). V is 1 J/bar for all materials. The viscosity of the lower mantle is set constant. UM is the upper mantle and TZ represents the transition zone.

Geological unit	Effective thickness		Geotherm	Viscosity	Friction coeff.	A_D	n	E
	[km]		[Myrs]	[Pa s]	[-]	[Pa s]	[-]	[J]
<u>Lithosphere</u>	<u>Crust</u>	<u>Mantle</u>						
Background	15		5	10^{18a}	0.020/0.005 ^c	$1.97 \cdot 10^{17}$	2.3	$1.54 \cdot 10^5$
Background		75	5	$10^{18}/10^{24b}$	0.600/0.400 ^c	$3.98 \cdot 10^{16}$	3.5	$5.32 \cdot 10^5$
Subducting oceanic+slab	15		150	$10^{18}/10^{24b}$	0.020/0.005 ^c	$1.97 \cdot 10^{17}$	2.3	$1.54 \cdot 10^5$
Subducting oceanic+slab		75	150	$10^{18}/10^{23b}$	0.600/0.400 ^c	$3.98 \cdot 10^{16}$	3.5	$5.32 \cdot 10^5$
Subducting continental	40		150	$10^{18}/10^{24b}$	0.150	$1.97 \cdot 10^{17}$	2.3	$1.54 \cdot 10^5$
Subducting continental		50	150	$10^{18}/10^{23b}$	0.600/0.400 ^c	$3.98 \cdot 10^{16}$	3.5	$5.32 \cdot 10^5$
Overriding continental	30		70	$10^{18}/10^{22b}$	0.010	$1.97 \cdot 10^{17}$	2.3	$1.54 \cdot 10^5$
Overriding continental		60	70	$10^{18}/10^{22b}$	0.200/0.100 ^c	$3.98 \cdot 10^{16}$	3.5	$5.32 \cdot 10^5$
Weak zones		90	150	10^{18}	0.600/0.400 ^c	-	-	-
UM+TZ		570	Adiabatic	$10^{18}/10^{24b}$	0.600/0.400 ^c	$3.98 \cdot 10^{16}$	3.5	$5.32 \cdot 10^5$
Lower mantle		40	Adiabatic	10^{23}	0.600/0.400 ^c	-	-	-

^ano upper cut-off due to small friction coeff.

^bupper/lower cut-off values

^clow/high strain

239 culate the fabrics. Following Boneh et al. (2015) we set the grain-boundary-mobility
240 (MOB, dimensionless) of olivine to 10, which yields weaker LPOs and associated seis-
241 mic anisotropy more consistent with observations. Anisotropy of deformed upper man-
242 tle aggregates is dominated by the transverse isotropy (TI) component (Becker, 2006),
243 where the olivine fast axis is parallel to the symmetry axis and the other two crystal-
244 lographic axes are perpendicular to it. As such, the elastic properties of anisotropic
245 aggregates are shown by plotting the symmetry axis of the TI component which is ex-
246 tracted automatically from the full elastic tensor by D-Rex.

248 2.3. Synthetic SKS splitting

249 Synthetic SKS splitting parameters are computed with FSTRACK (Becker, 2006)
250 at the final timestep, using the full elastic tensors of the upper mantle crystal aggregates,
251 vertically stacked below a given station (grid with 50 km spacing, down to 400 km in
252 the central area of the model). We compute the harmonic response of the vertical stack

253 of layers to an incident plane wave with 5° to the vertical, over a range of frequen-
 254 cies (0-25 Hz), to obtain a pulse seismogram via the inverse Fourier transform, using
 255 the method of Kennett (2009) with anisotropic extensions (Chapman & Shearer, 1989,
 256 and references therein). Band-pass filters from 0.1 to 0.3 Hz are then applied to con-
 257 struct synthetic seismograms in the SKS band (3.3 to 10 s). Successively, the splitting
 258 is determined with the cross-correlation method of (Menke & Levin, 2003). The SKS
 259 splitting parameters of each seismic station are obtained by averaging all the fast az-
 260 imuths and delay times measured by rotating the vertical stack of elastic tensors by 2°
 261 intervals around the y-axis.

262 **3. Results**

263 *3.1. Different model geometries and kinematics*

264 Although different parameters and material properties have been tested, a few se-
 265 lected and important models will be presented in this section (Fig. 4). In our best
 266 fitting model (T63, see, Supplementary Materials and Fig. 4a, b), the trench retreats by
 267 about 5cm/yr in a timespan of 22.1 Myrs, while the subduction rate is about 2.3 cm/yr.
 268 The retreat starts at 3.3 Myrs with a rate of about 4 cm/yr and a slab dipping angle of
 269 about $30\text{--}45^\circ$. Starting at about 10 Myrs to 14.6 Myrs the retreat becomes very strong
 270 (15 cm/yr), but at the same time the slab becomes more gentle (30°). A tear as well
 271 as a break-off in the slab were achieved by imposing weak zones. The tearing starts
 272 around 14.6 Myrs. The slab steepens again rapidly afterwards to about 60° , implying
 273 the roll-back of the slab becomes faster, while the retreating velocity of the trench slows
 274 down (≈ 2.6 cm/yr) until the last timestep. When arriving at the lower boundary of the
 275 model, the slab becomes horizontal and buckles. The overriding plate is extruding into
 276 the background lithosphere area with a counterclockwise motion after 12 Myrs. In the
 277 non-retreating subduction areas the dipping angle of the slab is about 45° . The colli-
 278 sion of the subducting and overriding continental plates occurs around 14 Myrs, while
 279 the break-off happens at about 4 Myrs.
 280 More than 80 models have been tested in this study. Very fast trench retreat rates (e.g.
 281 T14 ≈ 8 cm/yr, T54 ≈ 6 cm/yr) and late tearing (e.g. T54 at about 19 Myrs, after the

282 subducting slab reaches the right subducting continental plate) in earlier models were
 283 prevented by e.g. increasing the age of the subducting oceanic plate to 150 Myrs and
 284 decreasing the activation volume to 1 J/bar, while horizontal subduction of the slab was
 285 avoided by increasing the friction coefficients as well as brittle strain weakening. A
 286 lower rigidity and thus higher deformation of the upper continental plate was obtained
 287 by decreasing the viscosities upper cut-off value by two orders of magnitudes. The
 288 x-normal periodic boundary conditions were found to be critical in order to have a sus-
 289 tained slab roll-back. Initially, the z-domain was set to 2000 km, but mantle flow and
 290 strain could not evolve independently in the roll-back area without being influenced by
 291 surrounding regions. To achieve this, 500 km were added to the width of the back-arc
 292 domain (oceanic subducting and continental subducting plate respectively).
 293 Figure 4c shows the geodynamic result after 20.2 Myrs of a model (T80) without weak
 294 zones. The retreat of the trench is fast (≈ 7 cm/yr) and no detachment in the slab can be
 295 observed. The strong mantle flow through the tear is missing and the front part of the
 296 overriding plate appears to retreat very fast towards the right. The third model (T79)
 297 (Fig. 4e), with a wide overriding plate (strong continental crust) produces a steep slab
 298 without retreat, even after 28 Myrs years. The break-off in the top part of the model
 299 is achieved beneath a region where the weak zone is placed initially, although no tear
 300 propagation at the corner of the overriding continental plate and slab is observed.

301 *3.2. Mantle flow and viscosity/temperature field*

302 The overall trend of the direction of mantle flow in the upper mantle, which is es-
 303 timated at the end of the model evolution (model T63, Fig. 5, 6 and S1) underneath
 304 the subducting plate is parallel to the plate movement direction and becomes vertical
 305 when entrained at depth by the slab. As a result of the strongly retreating trench and the
 306 geometry of the plates, the overriding continental plate is laterally extruded towards the
 307 trench and the upper mantle flow below this plate is oriented counterclockwise at about
 308 25° with respect to the convergence direction. Subduction induces poloidal convective
 309 cells below and above the slab, with upwelling at the slab tip, horizontal corner flow in
 310 the transition zone and return flow underneath the slab. Such toroidal and poloidal flow
 311 components are locally perturbed in proximity of the break-off and tear areas where

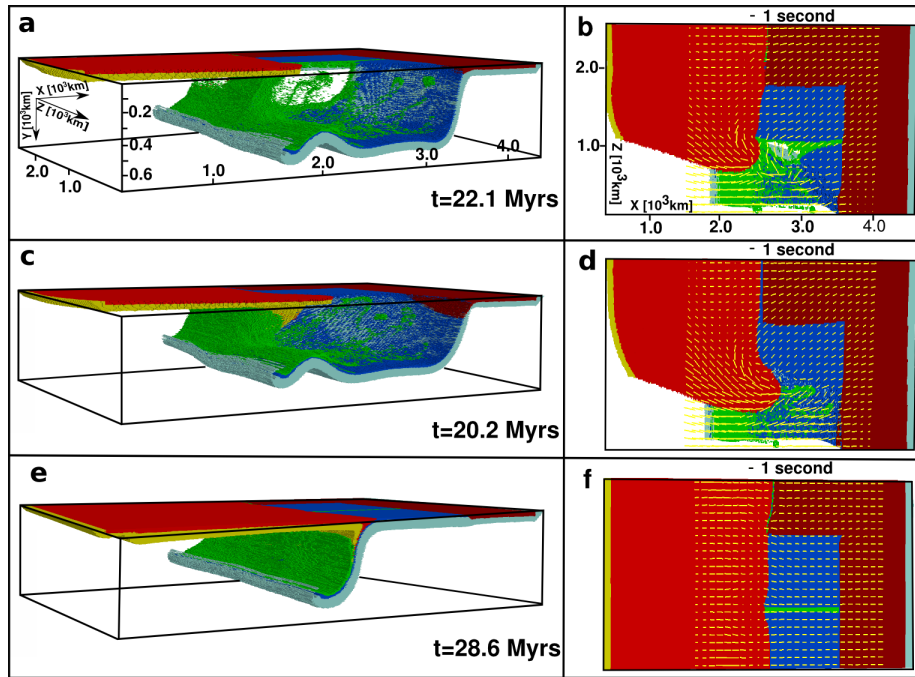


Figure 4: 3-D view of three different models and resulting SKS splitting parameters (yellow lines). a,b model with weak zones in the subducting oceanic plate (T63, best fit model). c,d model without weak zones (T80). e,f model with a strong uniform upper continental plate (T79).

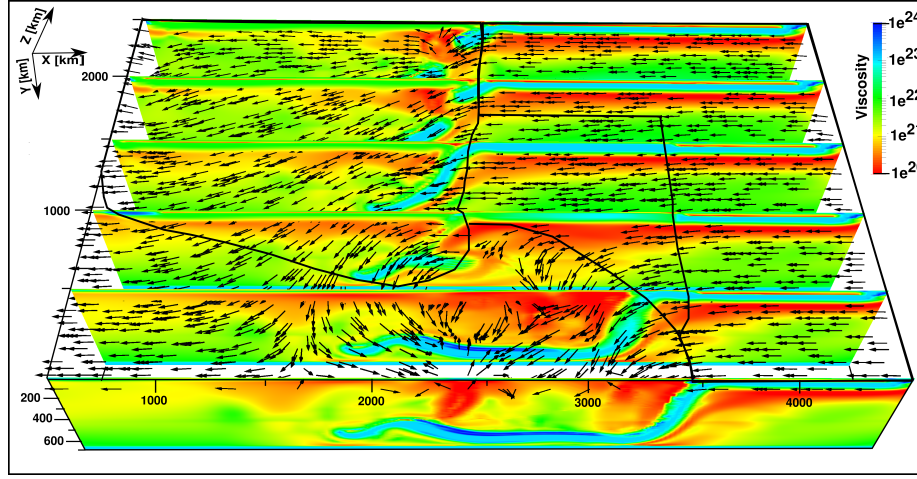


Figure 5: Viscosity field on six vertical slices along the x-plane with 500 km spacing at 22.1 Myrs of model T63. Arrows are scalars of the flow direction on a horizontal slice in 100 km depth. Black lines represent sketch of plate boundaries and trench.

the sub-slab mantle migrates fast toward the mantle wedge.

The viscosity (Fig. 5) is much lower in the mantle surrounding the sliding portions of subducting and overriding plates, owing to the employed non-Newtonian, strain rate dependent, rheology. Very low viscosity zones can be seen in the break-off and tearing area where the hot and actively deforming upper mantle penetrates in the mantle wedge through the slab window. The temperature field (Fig. 6) is more layer and depth dependent, owing to the adiabatic heating/cooling that suppresses thermal instabilities. Depth independent changes of temperature can be seen in proximity of the cold slab which is warming up very slowly. In the break-off and tear areas, hot material flows through the cold walls of the slab and heats the overlying mantle lithosphere. The mantle flow of T80 (Fig. 4c) is similar to model T63 (reference model), except that there is no inflow of subslab mantle into the mantle wedge. As a result of this, the poloidal component of mantle flow increases at the expenses of the toroidal component. The subduction-induced mantle flow of model T79 (Fig. 4e) above and below the slab is predominantly poloidal as the slab kinematics is constant along the trench. Differential retreat/advance of the slab is needed to generate horizontal (toroidal) mantle flow.

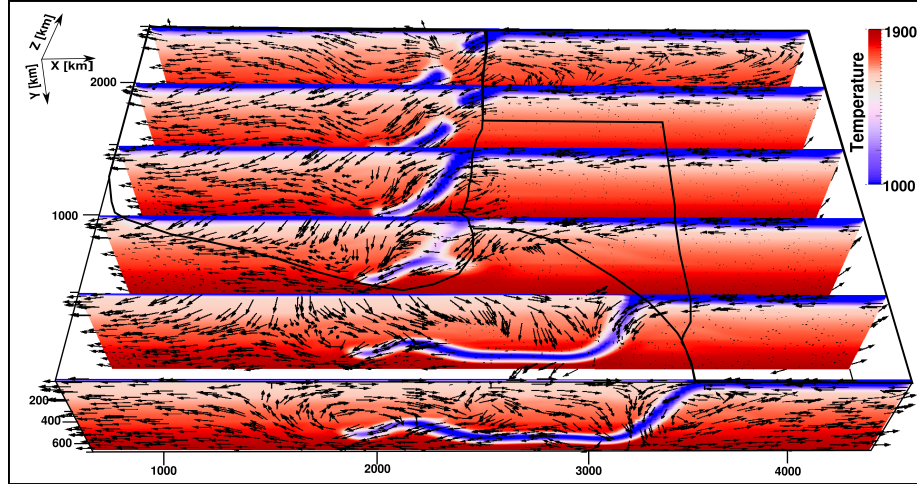


Figure 6: Temperature field in Kelvin and flow direction (arrows) on six vertical slices along the x-plane with 500 km spacing at 22.1 Myrs of model T63. Black lines represent sketch of plate boundaries and trench.

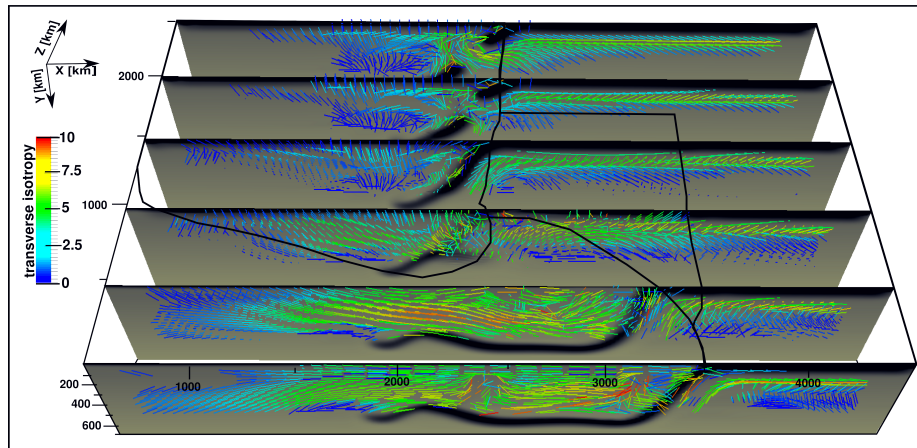


Figure 7: 50 km thick slices mapping temperatures from low to high values (black to grey, respectively) and transverse isotropy (the bars indicating the direction of the symmetry axis), with the schematic sketch of the plate boundaries (black lines) at 22.1 Myrs of model T63. The color and length of the bars is proportional to the amount of transverse isotropy.

3.3. Synthetic calculation of SKS anisotropy parameters

The strongest LPOs and related highest transverse isotropy in the upper mantle (10 %, up to ten times higher than its neighbouring regions, Fig. 7) can be seen in the area surrounding the retreating slab from the top, down to a depth of 410 km, while the poorly deforming slab is isotropic. Underneath the subducting oceanic and continental plate anisotropy changes from maximum 10 % in adjacent mantle levels to only 1 % in deeper layers and the general trend is trench-perpendicular. Anisotropy is higher in the break-off and tear zones (6-8 %). The symmetry axes are sub-parallel to the average orientation of the olivine fast axis (Faccenda & Capitanio, 2013) and to the mantle flow and strain directions.

SKS splitting parameters in our best model (T63) are mostly trench-perpendicular and show a circular pattern below the extruding overriding continental plate (Fig. 4b and 8). In the back-arc area very high TDs (up to 4 s) and trench-perpendicular FPDs exist, while splitting parameters closer to the trench are smaller ($TD < 1$ s) with inconsistent FPDs. The sub-horizontal mantle flow through the tear produces very strong ($TD = 2$ -3 s) FPDs perpendicular close to the trench, but oblique to the overall trend in the back-arc area. Near the edges of the tear, the FPDs are affected by the fast mantle flow and display a circular pattern and higher time delays (2-3.5 s) than the surrounding areas (0.5-2 s). Similarly, the strong mantle flow in relation to the break-off in the top part of the model controls SKS splitting parameters with FPDs oriented strictly parallel to the flow and higher time delays (~ 2 s) than surrounding regions (1 s). On the other hand, the break-off does not have such a strong impact, since the main direction of flow and strain is similar to the converging direction.

SKS splitting parameters of model T80 (Fig. 4d) are quite similar to T63, only the splitting parameters affected by the tear and the strong movement of the front part of the continental overriding plate differ. This can be seen in even stronger and more organised counterclockwise rotating splitting parameters. In model T79 the time delays are very small (about 1 s) and splitting parameters align mainly perpendicular to the trenches, exceptions are only close to the weak zones (Fig. 4f).

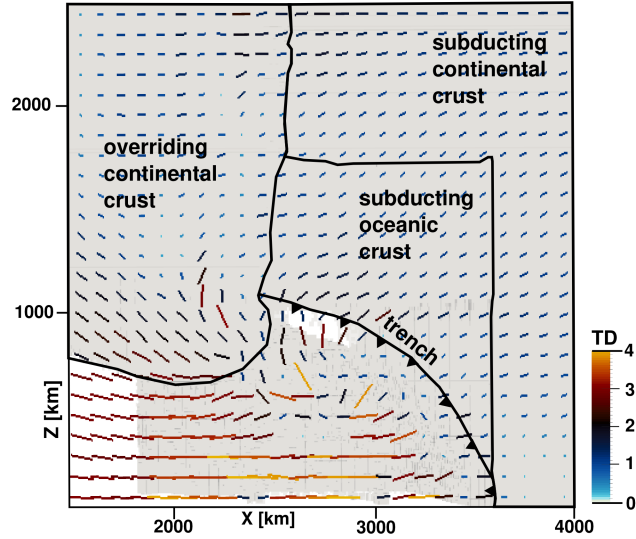


Figure 8: SKS splitting parameters in a selected central area in the model with a 50 km spacing station grid of model T63. Colorbar shows the delay time in seconds.

4. Discussion

4.1. Model set-up, evolution of plate movement and mantle flow

Our numerically computed geodynamic model convincingly simulates the evolution and current geological situation of the eastern Mediterranean in many aspects. We favour our interpretation of the best fitting model, T63 (Fig. 4a, b), which includes a slab tear, a slab break-off and a fast retreating trench, since the proofs of these features have been evident in various seismic imaging studies (e.g. seismic tomography, receiver functions, shear wave splitting measurements, surface waves analysis). The model dimensions differ from the actual present-day geometry in many areas. For instance, the Aegean Sea is just about 500 km wide in E-W direction, but for resolution and modelling reasons we had to make it 1000 km wide (see 3.1). This allowed the halfcircle of retreat to establish its independent mantle flow and strain region, less influenced by boundary conditions and nearby regions. On the other hand, the width of Anatolia represented by the overriding continental plate is 2000 km as being similar to its present-day dimensions. Here we should notice that we primarily focus on

373 the subduction systems and the outcome of mantle flow and anisotropy patterns and
 374 some adjustments had to be done to fit for example the resolution of the model and
 375 convergence rates. A change in geometries of the African and Arabian plates as well
 376 as the N-S width of the oceanic plate would not have a strong impact on mantle flow
 377 directions and splitting parameters since there has not been any drastic change of plate
 378 movement in the past 20 Myrs.

379 Recent strong extension in the Aegean (last 10-15 Myrs, Jolivet et al. (2013)) and a
 380 tear in the slab between the Hellenic and the Cyprus trench (15 Myrs ago, Dilek &
 381 Altunkaynak (2009); Jolivet et al. (2015)), amplifying roll-back, can be dated likewise
 382 in our model about 12 Myrs and 8 Myrs before the last timestep (blt), respectively. The
 383 fast extension 12 Myrs blt in our model triggers the tearing (8 Myrs blt), afterwards the
 384 tension between overriding plate and oceanic plate is released, as a consequence the
 385 retreat slows down and the slab angle steepens. As postulated by Taymaz et al. (1990)
 386 the slab is dipping northward, but is more fragmented, than in our study. The dip an-
 387 gle of the retreating slab (60°) is steeper than the one observed in tomography models
 388 Biryol et al. (2011). The slab becomes even steeper following the initiation of the tear-
 389 ing. Whereas the eastern continuation of the slab is dipping with an angle of 45° that
 390 is similarly resolved for the Cyprus slab of Biryol et al. (2011). Our model calculations
 391 date the collision of the continents in eastern Anatolia very late (8 Myrs blt). Thus
 392 comparing them with plate evolution models (e.g. Jolivet & Faccenna, 2000, about 30-
 393 35 Myrs ago) is difficult, due to the simplicity of starting models, that are supposed to
 394 involve the complicated history of long lasting subduction processes in the region. The
 395 break-off in the slab happens in our model at about 18 Myrs blt, which is earlier than in
 396 the literature (Keskin, 2003, 11-13 Myrs ago). These discrepancies arise from different
 397 subduction speeds and mechanism from west to east and combining them into a single
 398 model is difficult. However, we would like to notice here that our modelling study can
 399 provide important constraints on possible effects of these geodynamic events on mantle
 400 flow and strain history.

401 Our strong northward directed mantle flow velocity field through the break-off in east-
 402 ern Turkey, the movement of the plates and counterclockwise rotating velocity vectors
 403 towards south match the movement of the upper plates of an laboratory tests carried out

by Faccenna et al. (2006). Variations of our flow directions within the uppermost mantle (≈ 100 km) (Fig. 5 and S1) and plate movement from GPS measurements (Reilinger et al., 2006; Le Pichon & Kreemer, 2010) agree in many regions, especially the Aegean, western Anatolia and the Arabian plate. In central and eastern Anatolia GPS vectors appear to show roughly 30° of eastward deviation with respect to our mantle flow vectors at a depth of 100 km. This general consistency might be an indicator of a possible coupling between the crust and the uppermost mantle as earlier proposed by Göğüş & Pysklywec (2008), not just for eastern Anatolia but a larger region including central and western Anatolia and the Aegean. Starting at a depth of 300 km, mantle flow vectors are mostly oriented parallel to the subduction direction in Anatolia and affected strongly by the tearing and break-off, as well as toroidal corner flow with trench-parallel mantle flow underneath and behind the slab.

4.2. Selection of optimum model

Numerous models were tested searching for the best fitting rheological properties and plate tectonic features in the study region. Finally we decided on T63 as the optimum match following a weighting process between a realistic reconstruction and numerical modelling limitations. In this section we will discuss why we eliminated some other typical model setting for further interpretation.

A model without imposed weak zones (T80, Fig. 4c), to start detachment, but otherwise same rheological properties as the reference model T63, shows no sign of tearing or break-off. The impact on mantle flow and anisotropy, of missing slab openings, is only noticeable underneath these detachment areas. In T63 the tearing slows down the otherwise fast extrusion towards the trench, which seems to be too extreme in T80. A tear in the slab underneath western Anatolia (e.g. Jolivet et al., 2015; Govers & Fichtner, 2016) and a break-off in the slab in eastern Anatolia (e.g. Göğüş & Pysklywec, 2008; Faccenna et al., 2006) appear to be common features of the literature. Placing weak-zones might not represent a realistic geological scenario, due to unrealistic high friction coefficient and low viscosity parameters for crustal depths, but it seems to be an important modelling gadget, to reproduce detachment in the the slab.

Due to the absence of roll-back and tear initiation in the retreating area, model T79

(Fig. 4e) does not fit the recent evolution of the Aegean. For a good reconstruction of the mantle flow and strain in this region, the fast retreat is necessary, for higher TDs and toroidal flows. Inserting a thicker continental crust than in T63 might represent the crustal thickness of the Aegean (Tirel et al., 2004) better, but the numerical modelling implication is difficult. Therefore we decided to focus on the evolution of the mantle flow and anisotropy, rather than implementing the exact crustal dimensions.

4.3. Seismic anisotropy

The general pattern of the synthetic 3-D anisotropy calculations (Fig. 8), with a complex subduction model geometry and fitting parameters for the crust and upper mantle, imitating the eastern Mediterranean and Anatolian region, resemble to a first order, existing measured data in the area (Fig. 2 and 9). N-S (back-arc region/Aegean) to NE-SW (overriding/Anatolian plate) oriented FPDs are dominant over a broad area as observed in early SKS studies that have sampled eastern Turkey (e.g. Sandvol et al., 2003), north-central Turkey (Biryol et al., 2010), western Turkey (Paul et al., 2014), the Aegean Sea (Evangelidis et al., 2011; Confal et al., 2016) and along the Cyprus trench (Yolsal-Çevikbilen, 2014). Since symmetry (free-slip) conditions are applied to the front boundary ($z=0$) of the model, the trench is confined only in a half-arc, rather than the curved Hellenic trench. Thus, synthetically computed FPDs in the back-arc region are about $20\text{-}30^\circ$ more inclined towards north than those observed in most of the SKS studies.

The LPO simulations have several limitations, as for example they assume A-type olivine throughout the upper mantle domain, although melt, aqueous fluids and high stresses atop the subducting slab might favour the formation of different olivine fabrics (e.g. Jung et al., 2006) and/or the appearance of strongly anisotropic hydrous phases. Furthermore, the models do not take into account changes in creep mechanism and single crystal elastic properties as a function of the local pressure and temperature conditions which affect the seismic anisotropy signal. The D-Rex parameters have been calibrated with low strain deformation experiments (Kaminski et al., 2004, and references therein), but a comparison with high strain fabrics (e.g. Hansen et al., 2012) is still lacking. As a matter of fact, and similarly to what has been previously found

464 (Becker, 2006; Faccenda & Capitanio, 2013), a good fit between the synthetic data and
465 the observations is achieved when the mantle flow is sub-horizontal. This is because
466 the average orientation of the olivine fast axis is also horizontal, producing the largest
467 anisotropy contribution for the vertically travelling SKS wave. Altogether, these limi-
468 tations might be the principal reason for the overestimation of the TDs in the synthetic
469 Aegean area and for the poor fit of the SKS data around the trench where the vertical
470 component of flow is large.

471 We should also notice here that SKS-derived FPDs represent path-integrated average
472 anisotropy parameters over depth and time, and therefore might differ from mantle
473 flow directions. The anisotropy pattern in the Aegean is complicated and appears to
474 be affected by a layered structure with depth-varying anisotropic features. For a better
475 comparison, a well-resolved variation of vertically stratified azimuthal anisotropy that
476 could be inferred from the inversion of surface waves (e.g. Rayleigh waves) is neces-
477 sary. Such information has been available, until now, for a limited part of the study area
478 in Endrun et al. (2011) and must be expanded further to the north and east by covering
479 the entire Aegean and Turkey.

480 4.3.1. *Slab roll-back - Aegean back-arc region*

481 Splitting parameters with very high time delays (up to 4 s for synthetic vs. 2 s for
482 measured data) and trench-perpendicular FPDs can be observed in the area of the re-
483 treating slab, due to the existence of several or thick layers with identical FPDs increas-
484 ing the strength of anisotropy and thus time delays. The 2 s time delay discrepancies
485 between synthetic and observed time delays could be caused by several reasons: i)
486 our strain-induced mantle fabrics are too strong, indicating the active dislocation creep
487 at shallow depths (e.g. Karato et al., 2008), ii) upper mantle minerals become more
488 isotropic with depth, iii) a more complex mantle flow exists in the Aegean area as it
489 produces destructive interference among the different mantle layers. Other modelling
490 studies (e.g. Faccenna et al., 2013) estimated very small TDs (average 0.5 s) but similar
491 orientations, likely because of a minor amount of time-integrated deformation imposed
492 to develop the fabrics. Most recent studies considering a reliable amount of events ex-
493 hibit at least TDs of 1 s and higher (e.g. Paul et al., 2014; Confal et al., 2016).

494 Likewise anisotropic directions resolved after the anisotropic inversion of Rayleigh
 495 waves in Endrun et al. (2011), we identified significant N-S directed FPDs in the man-
 496 tle lithosphere of the North-Aegean Sea. Anisotropy patterns in the Aegean (strong
 497 TDs and trench-perpendicular FPDs) seem to be mainly controlled by corner flow, re-
 498 turn flow and high strain rates due to extensional conditions. The return flow in the
 499 sub-slab region and corner flow above the slab are very well resolved in our mantle
 500 flow model (Fig. 6, 9 and S1). The corner flow might be too strong and pushing the
 501 slab in a steeply dipping direction. The N-S directed FPDs in the back-arc region, com-
 502 pared to NE-SW FPDs in measured data, exist because free slip is applied to the sides
 503 of the model.

504 On the other hand, SKS splitting parameters in the fore-arc are smaller ($TD < 1$ s) and
 505 chaotic with some trench-parallel FPDs. Based on a globally compiled SKS splitting
 506 measurement data, Long & Silver (2009) reported that many subduction zone envi-
 507 ronments indicate a similar pattern. Yet, Faccenda & Capitanio (2013) more recently
 508 reported that this might only occur at narrow and retreating slabs. Since our system
 509 is retreating relatively fast and narrow this hypothesis would be reasonable. But only
 510 a few stations exhibit trench-parallel FPDs in the measured data (Evangelidis et al.,
 511 2011). However, these stations might be misleading according to Confal et al. (2016)
 512 due to the limited number of individual SKS observations (e.g. 3-4). Relatively small
 513 time delays close to the trench and seaward ($TD < 1$ s) could be due to the effect of
 514 differently oriented anisotropy in the mantle layers.

515

516 4.3.2. *Slab tear - western Anatolia*

517 As noticed by Paul et al. (2014), there is a change in south-western Anatolia to NW-
 518 SE oriented FPDs, due to the flow of asthenospheric material into the mantle wedge.
 519 This phenomena can be observed in the circular pattern at the edges of the tear and
 520 high TDs in our model as well. The location of the tear in the slab, regarding to Biryol
 521 et al. (2011), is further underneath the continental plate than in the geodynamic model
 522 of this study. But according to Govers & Fichtner (2016), the slab started tearing un-
 523 derneath Anatolia and then travelled southward, similarly to our modelled slab tearing,

524 which started underneath the lower margin of the upper continental crust (represent-
525 ing south-western Anatolia) and propagated toward the right boundary. Nevertheless,
526 calculated and measured splitting parameters show FPDs rotating from trench-normal
527 (central continental plate) to a counterclockwise pattern, at the edge of the tear, lead-
528 ing towards the back-arc area. The high heat flow associated with the vertical tear
529 in south-western Turkey could explain Late Miocene and Pliocene volcanism (Dilek
530 & Altunkaynak, 2009). Since then, extensional tectonics became more important for
531 magmatic activities than the slab tearing.

532 4.3.3. *Slab break-off - eastern Anatolia*

533 In eastern Turkey, the synthetic model of the mantle flow through the break-off in
534 the slab shows a significant contribution to the geodynamics of the region and higher
535 time delays point to strong mantle flow. Warmer material from beneath the slab in the
536 asthenosphere is transported to upper layers in the lithosphere (Fig. 6). The coverage of
537 splitting data in eastern Turkey is sparse, but Sandvol et al. (2003) and Paul et al. (2014)
538 showed that FPDs are mostly oblique (NE-SW) towards the Bitlis-Zagros Suture zone
539 and normal in the East due to the curvature of the suture zone, while our model data
540 is N-S directed and strictly perpendicular to the suture zone. Such difference could be
541 associated to the boundary conditions of our model (free slip normal to z and periodic
542 normal to x) or to the larger-scale mantle flow dynamics resulting from the effect of
543 existence of a broader Arabian-Eurasian collision zone, which is not modelled in this
544 study. The consistency of observed and synthetic SKS splitting data and the mismatch
545 between anisotropic orientations and surface features along the suture zone support
546 the idea that the anisotropy in the region is related to ongoing deformation in the as-
547 thenosphere, rather than representing fossil anisotropy in mantle lithosphere (Babuska
548 & Cara, 1991). The change of N-S directed mantle flow south of the suture zone to
549 NW-SE (similar to Capitanio (2016)) and low viscosities could explain the westward
550 escape of the Anatolian microplate (Fig. 5, 6 and S1). This does not mean that there
551 could not be any pull due to the roll-back in the Aegean, but rather that they might
552 be connected. Further anisotropic modelling, including vertical stratification of lay-
553 ers, is required in this region to better constrain strain-induced LPO in the past or at

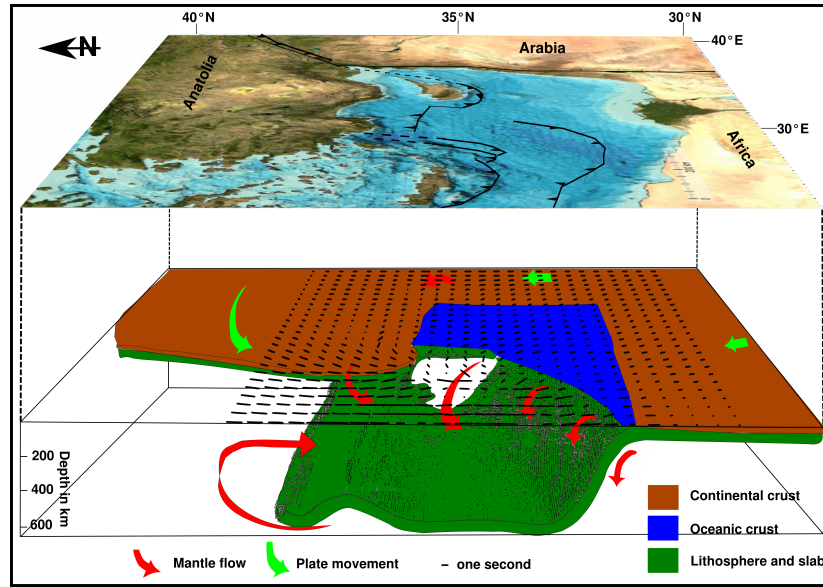


Figure 9: Geodynamic interpretation and modelled SKS splitting parameters (black lines, scale in 1 s) at the last timestep with the present-day map view of the eastern Mediterranean on top (GeoMapApp, <http://www.geomapapp.org>). Important tectonic features are represented in the map view with a rough sketch. Red arrows represent the mantle flow interpreted from this study and green arrows show the plate movement.

554 present. Nevertheless, the flow through the break-off could explain volcanism, domal
 555 uplift, heating and extension as described in several studies (e.g. Keskin, 2003; Göğüş
 556 & Pysklywec, 2008; Fichtner et al., 2013; Govers & Fichtner, 2016).

557 Our results show a good accordance with alternative anisotropic modelling study of
 558 Faccenna et al. (2013) covering a larger region, but our modelling study adds more
 559 details especially in western and central Anatolia.

560

561 5. Conclusion

562 Upper mantle anisotropy and synthetic SKS splitting parameters were calculated
 563 with three different algorithms (I3MG, D-REX and FSTRACK) by modelling the 3-
 564 D geodynamics of the eastern Mediterranean and Anatolian subduction systems, the

565 strain-induced LPO in the upper mantle and seismic wave propagation. We show that
 566 this combination of calculations can achieve SKS splitting parameters similar to ob-
 567 served data. Below the extruding Anatolian plate, the general FPDs are NE-SW di-
 568 rected, and circular around the tear in the slab, while strong splitting can be noticed in
 569 the Aegean region.

570 Differences between synthetic SKS splitting parameters and real data could be ascribed
 571 to the imposed model geometry and boundary conditions, potential effects related to
 572 larger-scale flow patterns and/or nearby subduction systems and different rheological
 573 parameters which control plastic deformation of upper mantle minerals. As an exam-
 574 ple, the presence of a highly fragmented slab would substantially affect on a local scale
 575 the geology and seismic anisotropy parameters.

576 Nevertheless, our study demonstrates that this type of combined simulations can repro-
 577 duce to a first order the time-dependent 3-D patterns of mantle convection and resulting
 578 seismic anisotropy is mainly consistent with measured observations. In this study we
 579 reproduce the present-day anisotropy patterns in the Aegean Sea, around the Cyprus
 580 trench as well as in Anatolia.

581 **6. Data and Resources**

582 Geodynamic simulations were performed on Galileo Computing Cluster, CINECA,
 583 Italy. The I3MG (Gerya, 2009) code was used for the geodynamic modelling, D-
 584 Rex (Kaminski et al., 2004) for the fabric modelling and FSTRACK (Becker, 2006)
 585 to calculate SKS splitting parameters. Paraview was used for graphic visualization
 586 (<https://www.paraview.org/>). Data from prior SKS splitting measurements
 587 were taken from Wüstefeld & Bokelmann (2007). The figures are generated using
 588 the Generic Mapping Tools software (GMT, [http://gmt.soest.hawaii.edu/](http://gmt.soest.hawaii.edu/projects/gmt)
 589 [projects/gmt](http://gmt.soest.hawaii.edu/projects/gmt)) and Inkscape.

590 **7. Acknowledgements**

591 This study is funded by the National Scientific and Technological Research Coun-
 592 cil of Turkey (TÜBİTAK), project no: ÇAYDAG-115Y248. We are thankful to the

University of Padova, Italy, for supporting the research, with the permission for the use of the Galileo Computing Cluster, CINECA. We thank the Turkish Academy of Sciences (TÜBA) in the framework for Young Scientist Award Program (TÜBA-GEBİP) and the Alexander von Humboldt Foundation Research Fellowship Award for financial support and for further providing computing facilities and other relevant resources through Humboldt-Stiftung Follow-Up Programme. This paper has benefited from the review of A. Menant and an anonymous reviewer.

References

- Babuska, V., & Cara, M. (1991). *Seismic anisotropy in the Earth* volume 10. Springer Science & Business Media.
- Becker, T. W. (2006). On the effect of temperature and strain-rate dependent viscosity on global mantle flow, net rotation, and plate-driving forces. *Geophysical Journal International*, 167, 943–957.
- Biryol, C. B., Beck, S. L., Zandt, G., & Özacar, A. A. (2011). Segmented African lithosphere beneath the Anatolian region inferred from teleseismic P-wave tomography. *Geophysical Journal International*, 184, 1037–1057.
- Biryol, C. B., Zandt, G., Beck, S. L., Ozacar, A. A., Adiyaman, H. E., & Gans, C. R. (2010). Shear wave splitting along a nascent plate boundary: the North Anatolian Fault Zone. *Geophysical Journal International*, 181, 1201–1213.
- Boneh, Y., Morales, L. F., Kaminski, E., & Skemer, P. (2015). Modeling olivine CPO evolution with complex deformation histories: Implications for the interpretation of seismic anisotropy in the mantle. *Geochemistry, Geophysics, Geosystems*, 16, 3436–3455.
- Capitanio, F. A. (2016). The role of the miocene-to-pliocene transition in the eastern mediterranean extrusion tectonics: Constraints from numerical modelling. *Earth and Planetary Science Letters*, 448, 122–132.

619 Chapman, C., & Shearer, P. (1989). Ray tracing in azimuthally anisotropic media-II.
620 Quasi-shear wave coupling. *Geophysical Journal International*, 96, 65–83.

621 Confal, J. M., Eken, T., Tilmann, F., Yolsal-Çevikbilen, S., Çubuk-Sabuncu, Y., Saygin,
622 E., & Taymaz, T. (2016). Investigation of mantle kinematics beneath the Hellenic-
623 subduction zone with teleseismic direct shear waves. *Physics of the Earth and Plan-
624 etary Interiors*, 261, 141–151.

625 Connolly, J. A. (2005). Computation of phase equilibria by linear programming: a
626 tool for geodynamic modeling and its application to subduction zone decarbonation.
627 *Earth and Planetary Science Letters*, 236, 524–541.

628 Çubuk-Sabuncu, Y., Taymaz, T., & Fichtner, A. (2017). 3-D crustal velocity structure
629 of western Turkey: Constraints from full-waveform tomography. *Physics of the
630 Earth and Planetary Interiors*, 270, 90–112.

631 Dilek, Y., & Altunkaynak, Ş. (2009). Geochemical and temporal evolution of Ceno-
632 zoic magmatism in western Turkey: mantle response to collision, slab break-off,
633 and lithospheric tearing in an orogenic belt. *Geological Society, London, Special
634 Publications*, 311, 213–233.

635 Endrun, B., Lebedev, S., Meier, T., Tirel, C., & Friederich, W. (2011). Complex layered
636 deformation within the Aegean crust and mantle revealed by seismic anisotropy.
637 *Nature geoscience*, 4, 203–207.

638 Evangelidis, C. (2017). Seismic anisotropy in the Hellenic subduction zone: Effects
639 of slab segmentation and subslab mantle flow. *Earth and Planetary Science Letters*,
640 480, 97–106.

641 Evangelidis, C., Liang, W.-T., Melis, N., & Konstantinou, K. (2011). Shear wave
642 anisotropy beneath the Aegean inferred from SKS splitting observations. *Journal of
643 Geophysical Research: Solid Earth* (1978–2012), 116.

644 Faccenda, M. (2014). Mid mantle seismic anisotropy around subduction zones. *Physics
645 of the Earth and Planetary Interiors*, 227, 1–19.

646 Faccenda, M., & Capitanio, F. (2013). Seismic anisotropy around subduction zones:
647 Insights from three-dimensional modeling of upper mantle deformation and SKS
648 splitting calculations. *Geochemistry, Geophysics, Geosystems*, 14, 243–262.

649 Faccenna, C., Becker, T. W., Jolivet, L., & Keskin, M. (2013). Mantle convection in
650 the Middle East: Reconciling Afar upwelling, Arabia indentation and Aegean trench
651 rollback. *Earth and Planetary Science Letters*, 375, 254–269.

652 Faccenna, C., Bellier, O., Martinod, J., Piromallo, C., & Regard, V. (2006). Slab de-
653 tachment beneath eastern Anatolia: A possible cause for the formation of the North
654 Anatolian fault. *Earth and Planetary Science Letters*, 242, 85–97.

655 Faccenna, C., Jolivet, L., Piromallo, C., & Morelli, A. (2003). Subduction and the
656 depth of convection in the Mediterranean mantle. *Journal of Geophysical Research:*
657 *Solid Earth*, 108.

658 Fichtner, A., Saygin, E., Taymaz, T., Cupillard, P., Capdeville, Y., & Trampert, J.
659 (2013). The deep structure of the North Anatolian fault zone. *Earth and Planetary*
660 *Science Letters*, 373, 109–117.

661 Gerya, T. (2009). *Introduction to numerical geodynamic modelling*. Cambridge Uni-
662 versity Press.

663 Göğüş, O. H., & Pysklywec, R. N. (2008). Mantle lithosphere delamination driving
664 plateau uplift and synconvergent extension in eastern Anatolia. *Geology*, 36, 723–
665 726.

666 Govers, R., & Fichtner, A. (2016). Signature of slab fragmentation beneath Anatolia
667 from full-waveform tomography. *Earth and Planetary Science Letters*, 450, 10–19.

668 Hansen, L., Zimmerman, M., & Kohlstedt, D. (2012). Laboratory measurements of the
669 viscous anisotropy of olivine aggregates. *Nature*, 492, 415.

670 Jolivet, L., & Faccenna, C. (2000). Mediterranean extension and the Africa-Eurasia
671 collision. *Tectonics*, 19, 1095–1106.

672 Jolivet, L., Faccenna, C., Huet, B., Labrousse, L., Le Pourhiet, L., Lacombe, O.,
673 Lecomte, E., Burov, E., Denele, Y., Brun, J.-P. et al. (2013). Aegean tectonics:
674 Strain localisation, slab tearing and trench retreat. *Tectonophysics*, 597, 1–33.

675 Jolivet, L., Menant, A., Sternai, P., Rabillard, A., Arbaret, L., Augier, R., Laurent, V.,
676 Beaudoin, A., Grasemann, B., Huet, B. et al. (2015). The geological signature of a
677 slab tear below the Aegean. *Tectonophysics*, 659, 166–182.

678 Jung, H., Katayama, I., Jiang, Z., Hiraga, T., & Karato, S.-I. (2006). Effect of water
679 and stress on the lattice-preferred orientation of olivine. *Tectonophysics*, 421, 1–22.

680 Kaminski, E., Ribe, N. M., & Browaeys, J. T. (2004). D-Rex, a program for calculation
681 of seismic anisotropy due to crystal lattice preferred orientation in the convective
682 upper mantle. *Geophysical Journal International*, 158, 744–752.

683 Karato, S.-i., Jung, H., Katayama, I., & Skemer, P. (2008). Geodynamic significance of
684 seismic anisotropy of the upper mantle: new insights from laboratory studies. *Annu.*
685 *Rev. Earth Planet. Sci.*, 36, 59–95.

686 Kennett, B. (2009). *Seismic wave propagation in stratified media*, Cambridge Univer-
687 sity. ANU E Press.

688 Keskin, M. (2003). Magma generation by slab steepening and breakoff beneath a
689 subduction-accretion complex: An alternative model for collision-related volcanism
690 in Eastern Anatolia, Turkey. *Geophysical Research Letters*, 30.

691 Kind, R., Eken, T., Tilmann, F., Sodoudi, F., Taymaz, T., Bulut, F., Yuan, X., Can, B., &
692 Schneider, F. (2015). Thickness of the lithosphere beneath Turkey and surroundings
693 from S-receiver functions. *Solid Earth*, 6, 971.

694 Le Pichon, X., & Kreemer, C. (2010). The Miocene-to-present kinematic evolution
695 of the eastern Mediterranean and Middle East and its implications for dynamics.
696 *Annual Review of Earth and Planetary Sciences*, 38, 323–351.

697 Long, M. D., & Silver, P. G. (2009). Mantle flow in subduction systems: The subslab
698 flow field and implications for mantle dynamics. *Journal of Geophysical Research:*
699 *Solid Earth (1978–2012)*, 114.

- 700 Menant, A., Sternai, P., Jolivet, L., Guillou-Frottier, L., & Gerya, T. (2016). 3D numerical
701 modeling of mantle flow, crustal dynamics and magma genesis associated with
702 slab roll-back and tearing: The eastern Mediterranean case. *Earth and Planetary
703 Science Letters*, 442, 93–107.
- 704 Menke, W., & Levin, V. (2003). The cross-convolution method for interpreting SKS
705 splitting observations, with application to one and two-layer anisotropic earth models.
706 *Geophysical Journal International*, 154, 379–392.
- 707 Mutlu, A. K., & Karabulut, H. (2011). Anisotropic Pn tomography of Turkey and
708 adjacent regions. *Geophysical Journal International*, 187, 1743–1758.
- 709 Olive, J.-A., Pearce, F., Rondenay, S., & Behn, M. D. (2014). Pronounced zonation
710 of seismic anisotropy in the Western Hellenic subduction zone and its geodynamic
711 significance. *Earth and Planetary Science Letters*, 391, 100–109.
- 712 Park, J., & Levin, V. (2002). Seismic anisotropy: tracing plate dynamics in the mantle.
713 *Science*, 296, 485–489.
- 714 Pasyanos, M. E., & Walter, W. R. (2002). Crust and upper-mantle structure of North
715 Africa, Europe and the Middle East from inversion of surface waves. *Geophysical
716 Journal International*, 149, 463–481.
- 717 Paul, A., Karabulut, H., Mutlu, A. K., & Salaün, G. (2014). A comprehensive and
718 densely sampled map of shear-wave azimuthal anisotropy in the Aegean–Anatolia
719 region. *Earth and Planetary Science Letters*, 389, 14–22.
- 720 Ranalli, G. (1995). *Rheology of the Earth*. Springer Science & Business Media.
- 721 Reilinger, R., McClusky, S., Vernant, P., Lawrence, S., Ergintav, S., Cakmak, R.,
722 Ozener, H., Kadirov, F., Guliev, I., Stepanyan, R. et al. (2006). GPS constraints
723 on continental deformation in the Africa-Arabia-Eurasia continental collision zone
724 and implications for the dynamics of plate interactions. *Journal of Geophysical Research: Solid Earth*, 111. B05411.
725

- 726 Sandvol, E., Turkelli, N., Zor, E., Gok, R., Bekler, T., Gurbuz, C., Seber, D., &
727 Barazangi, M. (2003). Shear wave splitting in a young continent-continent colli-
728 sion: An example from eastern Turkey. *Geophysical Research Letters*, 30.
- 729 Sternai, P., Jolivet, L., Menant, A., & Gerya, T. (2014). Driving the upper plate surface
730 deformation by slab rollback and mantle flow. *Earth and Planetary Science Letters*,
731 405, 110–118.
- 732 Taymaz, T. (1996). S-P-wave traveltime residuals from earthquakes and lateral inho-
733 mogeneity in the upper mantle beneath the Aegean and the Hellenic Trench near
734 Crete. *Geophysical Journal International*, 127, 545–558.
- 735 Taymaz, T., Jackson, J., & Westaway, R. (1990). Earthquake mechanisms in the Hel-
736 lenic Trench near Crete. *Geophysical Journal International*, 102, 695–731.
- 737 Tirel, C., Gueydan, F., Tiberi, C., & Brun, J.-P. (2004). Aegean crustal thickness
738 inferred from gravity inversion. Geodynamical implications. *Earth and Planetary
739 Science Letters*, 228, 267–280.
- 740 Van Hinsbergen, D. J. J., Hafkenscheid, E., Spakman, W., Meulenkaamp, J., & Wortel,
741 R. (2005). Nappe stacking resulting from subduction of oceanic and continental
742 lithosphere below Greece. *Geology*, 33, 325–328.
- 743 Vanacore, E., Taymaz, T., & Saygin, E. (2013). Moho structure of the Anatolian Plate
744 from receiver function analysis. *Geophysical Journal International*, 193, 329–337.
- 745 Wortel, M., & Spakman, W. (2000). Subduction and slab detachment in the
746 Mediterranean-Carpathian region. *Science*, 290, 1910–1917.
- 747 Wüstefeld, A., & Bokelmann, G. (2007). Null detection in shear-wave splitting mea-
748 surements. *Bulletin of the Seismological Society of America*, 97, 1204–1211.
- 749 Yolsal-Çevikbilen, S. (2014). Seismic anisotropy along the Cyprean arc and northeast
750 Mediterranean Sea inferred from shear wave splitting analysis. *Physics of the Earth
751 and Planetary Interiors*, 233, 112–134.

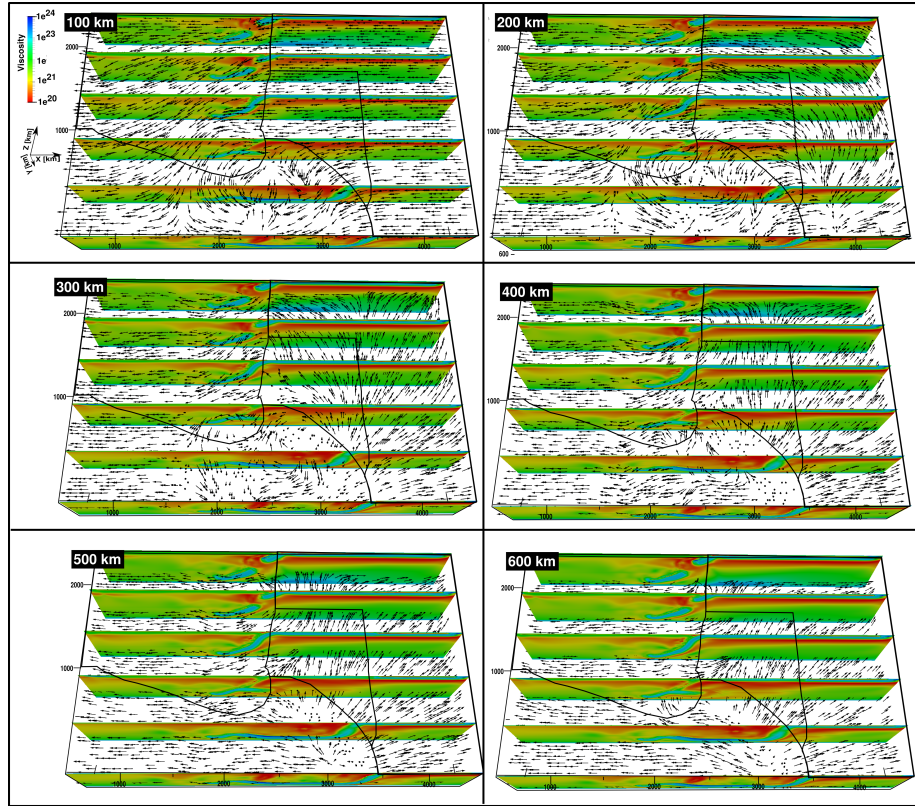


Figure S1: Six figures of the viscosity field on six vertical slices along the x-plane with 500 km spacing at 22.1 Myrs of model T63. Arrows are scalars of the flow direction on horizontal slices in 100-600 km depth. Black lines represent sketch of plate boundaries and trench.

8. Supplementary

In this section additional geodynamic modelling results are provided. Figure S1 shows the depth dependent mantle flow on horizontal slices and the viscosity on vertical slices. Three movies of the models discussed above show the time evolution of the models from the initial to the last episode.